Tribological performance assessment of Al2O3-YSZ composite coatings deposited by hybrid powder-suspension plasma spraying

N.B. When citing this work, cite the original published paper.

(article starts on next page)

Tribological performance assessment of Al$_2$O$_3$-YSZ composite coatings deposited by hybrid powder-suspension plasma spraying

Ashish Ganvir [a,*], Sneha Goel [a], Sivakumar Govindarajan [b], Adwait Rajeev Jahagirdar [a], Stefan Björklund [a], Uta Klement [c], Shrikant Joshi [a]

[a] University West, 461832 Trollhättan, Sweden
[b] International Advanced Research Centre for Powder Metallurgy and New Materials (ARCI), 500005 Hyderabad, India
[c] Chalmers University of Technology, Gothenburg, Sweden

ARTICLE INFO

ABSTRACT

The advent of high-throughput plasma spray systems that allow axial feeding encourages the study of using liquid feedstock for various next-generation functional applications. The current study explores the benefit of such a plasma spray system to deposit hybrid powder-suspension Al$_2$O$_3$-YSZ ceramic matrix composite (CMC) coatings for tribological applications. The tribological performance of the hybrid processed CMC coatings was assessed using scratch, ball-on-plate wear and erosion tests and compared with that of monolithic powder-derived Al$_2$O$_3$ coatings. As-deposited and tribo-tested coatings were characterized using Scanning Electron Microscopy, X-ray Diffraction and Energy Dispersive Spectroscopy to analyse their microstructure and phase constitution. The results showed that the tribological performance of the hybrid powder-suspension Al$_2$O$_3$-YSZ CMC coating was significantly improved by enhancing the wear resistance under scratch, dry sliding ball-on-plate and erosion tests as compared to the conventional APS deposited monolithic Al$_2$O$_3$ coating. About 36% decrease in the dry sliding ball-on-plate specific wear rate and up to 50% decrease in the erosion wear rate was noted in the hybrid powder-suspension Al$_2$O$_3$-YSZ CMC coating as compared to the conventional APS deposited monolithic Al$_2$O$_3$ coating. The study concludes that the hybrid powder-suspension route can create CMC coatings with unique multi-length scale microstructures which can be attractive for combining different tribological attributes in the same coating system.

1. Introduction

Atmospheric plasma spraying (APS) is the most widely adopted thermal spray technology to deposit coatings for various functional applications such as corrosion, wear, thermal barrier, fuel cells etc. [1–4]. Deposition of a variety of feedstock materials such as metals, ceramics, cermets, intermetallics etc. is possible using APS where coarse powder particles (10–100 μm) are conveyed using a carrier gas such as Argon and injected into the hot plasma plume [5–8]. The particles are melted and accelerated towards the substrate resulting in partially or fully molten particles which form splats, and the subsequent deposition of splats lead to the formation of a coating. More recently, the idea of feeding fine (<1–3 μm) powder particles into the plasma plume to create fine-structured coatings has garnered increasing interest. This is due to the fact that the refined microstructures have been shown to outperform

the coatings resulting from conventional coarse spray-grade powders in various aspects such as wear, erosion, mechanical strength, thermal diffusivity [9–12] etc. However, this has required researchers to adapt the conventional APS technology suitably, since processing of fine particles (<1–3 μm) by the conventional APS approach, particularly when the feedstock is injected radially, i.e., perpendicular to the direction of the plasma plume, using traditional low power plasma torches is immensely challenging. The challenges are primarily associated with the inadequate momentum of the fine powder particles to penetrate the viscous plasma plume, and agglomeration of the fine powder particles leading to poor flowability and clogging of the injector nozzle [1].

Several attempts have been made to address the above challenges by pre-processing the fine powder particles via agglomeration and sintering routes [1,13,14]. However, such an approach not only requires close process control and monitoring during agglomeration and sintering

which are both time and resource demanding, but can also lead to the presence of non-molten and/or semi-molten particles in the deposited coating, leading to an adverse impact on coating performance [14,15]. An emerging alternative approach is to use suspensions where fine powder particles are suspended in water or ethanol prior to spraying. The processing of such suspensions using plasma spraying is termed as suspension plasma spraying (SPS), where the suspension is fed into the plasma plume either radially or axially. Although radial injection has been most widely utilized in plasma spraying [9,16], the use of axial injection is gaining more attention as it allows better thermal exchange between the plasma plume and the injected feedstock [17,18]. The axial injection becomes even more desirable when a suspension feedstock is used, because a significant amount of heat is consumed in evaporating the solvent and better thermal exchange and higher plasma power levels allow complete melting of the fine solute powder particles despite the above [19]. The processing of suspension via axial injection using plasma spraying is termed as axial suspension plasma spraying (ASPS).

The challenges associated with spraying of fine powder particles through APS and the latest advancement in axial feedstock injection systems has led to exploration of a hybrid spraying approach involving axial injection of both a conventional spray grade powder and a suspension carrying a fine powder to generate different function-dependent coating architectures and coatings with multi-length scale microstructures [20]. Despite the considerable potential of hybrid processing, there are only few prior studies on this subject where a combination of powder and suspension/solution is used, especially via axial injection route [20–24]. The hybrid processing concept via axial injection route using suspension and powder was first demonstrated by Björklund et al. [20] to produce various function-dependent coating architectures. The concept was further explored by Mistri et al. [25] and Mahade et al. [26] to demonstrate the deposition of metal matrix Tribaloy T400 composite coatings for wear applications. The similar concept was also utilized by Gopal et al. [27] and Murray et al. [28] to demonstrate the deposition of ceramic matrix alumina composite coatings for sliding wear under bovine serum solution and dry sliding wear application, respectively. This work is an attempt to further explore such a hybrid processing route deposited dual phase 'Al$_2$O$_3$' ceramic matrix composite (CMC) coatings reinforced with a fine scale second phase '8YSZ' under dry sliding wear, scratch wear as well as erosive wear conditions.

Dual phase/composite coatings have been of interest in view of their potential to provide better performance over corresponding single constituent material coatings. Improvement in mechanical behaviour by introduction of finely distributed second phase(s) (with the first phase being the coating matrix) can be attributed to the action of the latter as the crack arrestor and the crack-deviating characteristics of the inter-laminate interfaces [29]. Fine structured composite coatings with a multi-scale structure, i.e., presence of both micron- and fine-sized features, in particular, have shown improved performance over conventional coatings with micron-sized features [28]. A previous study on Al$_2$O$_3$-ZrO$_2$ fine-structured composite coating consisting of nano-sized ZrO$_2$ dispersed in micron-sized Al$_2$O$_3$ matrix has shown better wear resistance and lower friction coefficient in comparison with conventional Al$_2$O$_3$ coating [30]. Al$_2$O$_3$/ZrO$_2$ laminated composites produced by Berghaus et al. [29] have shown significant increase in mechanical and thermal performance of the composite coatings in comparison with YSZ coating, which can be useful for a variety of applications demanding enhanced resistance against abrasion, wear, oxygen diffusion, heat, etc.

It is also relevant to mention that zirconia toughened alumina (ZTA), an important manufacturing ceramic, has been extensively studied for decades both as a structural material as well as a protective coating as it can provide a combination of high hardness and Young's modulus of the Al$_2$O$_3$ matrix with an additional toughening effect resulting from the ZrO$_2$ dispersion, thereby significantly increasing the flexural strength and fracture toughness of Al$_2$O$_3$ [31–33]. For instance, kern et al. reported significantly higher Vickers hardness (up to 1900 HV$_{10}$) and fracture toughness (up to 3.6 MPa$\sqrt{m}$) in a alumina–10 vol% zirconia composite coating [34]. Similarly, Sommar et al., also reported a superior fracture toughness i.e., up to 4.3 MPa$\sqrt{m}$ in a alumina-24 vol% zirconia composite coating [35]. Such an enhanced hardness and fracture toughness was reported to be the primary reason for the improved tribological performance of the alumina-YSZ composite coatings [34–36]. Krishnamurthy et al., studied the influence of microhardness on wear resistance and found that the at 5 N load, the wear rate decreased by nearly 58% from 2.6 ($\times 10^{-3}$ mm^3/Nm) to 1.1 ($\times 10^{-3}$ mm^3/Nm) as the coating hardness increased by only 4.5% from 1000HV$_{0.1}$ to 1045HV$_{0.1}$ [36]. It should be borne in mind that the above studies have prompted the Al$_2$O$_3$-ZrO$_2$ system to be used as a case study to establish the possibility of depositing composite coatings by the hybrid processing route.

Processing of CMCs comprising constituents with diverse melting characteristics such as the Al$_2$O$_3$ and ZrO$_2$ is challenging to process under conventional deposition route and the challenge alleviates even further if an order of magnitude difference exists between the size of the two feedstocks utilized to process CMCs. However, hybrid processing route has shown the potential to overcome these challenges as demonstrated in the literature [20,24,27,28].

Therefore, the current study deals with deposition of multi length scale wear resistant Al$_2$O$_3$-YSZ CMC coatings via hybrid processing route using axial plasma spraying. A monolithic alumina coating was also deposited under similar processing conditions as a reference coating. Monolithic alumina coatings are most commonly used in industry due to their superior tribological properties, high hardness, high strength and high fracture toughness [37]. Both the CMC as well as the monolithic coatings were assessed at ambient conditions using scratch test, ball-on-disk wear test and erosion test. Furthermore, the coatings were also characterized using scanning electron microscopy (SEM), energy dispersive X-ray spectroscopy (EDS) and X-ray diffraction (XRD) to analyse their microstructure and phases.

2. Materials and methods

2.1. Feedstock, coating deposition & characterization

The feedstocks used in this study were a) a commercially available 25 wt% solid loaded suspension of YSZ in ethanol (AuerCoat® YSZ Suspension, d10 = 230 nm, d50 = 440 nm, d90 = 950 nm, Treibacher Industries AG, Austria) and b) spray-grade powder of Al$_2$O$_3$ (AMPERIT® 740, fused and crushed, 22/5 μm, H.C. Starck GmbH, Germany) with morphology as shown in Fig. 1(a) and (b), respectively.

The substrate used in this study was Domex 355 steel for depositing both the composite as well as monolithic coatings. Two types of substrate geometries, i.e., round buttons (⌀25 mm * 6 mm) and rectangular plates (60 mm * 20 mm) were used to facilitate subsequent characterization and production of specimens for tribological testing, respectively. Both the coatings were deposited using a Mettech Axial III high power plasma torch (Northwest Mettech Corp., Vancouver, Canada) equipped with Nanofeed 350 suspension feeder as well as a separate powder feed system (Uniquecoat, model PF50WL, Richmond, USA), as shown in the schematic in Fig. 2. The process parameters employed were similar (see Table 1) for both the coatings except the number of plasma torch passes. The composite coatings were deposited using simultaneous injection of Al$_2$O$_3$ powder and YSZ suspension with varied suspension feed rates corresponding to 5, 10, 15, and 20 wt% YSZ content in the hybrid powder-suspension feedstock.

Surface roughness of both the composite and monolithic coatings was measured using a surface profilometer (MITUTOYO SURFTEST-301) which records the movement of a stylus as it is dragged along the surface of the coating. Five readings were recorded for each specimen and average values with appropriate standard deviation are reported herein.

Polished cross-section sample preparation for microstructural investigation was done firstly by vacuum impregnating the as-sprayed
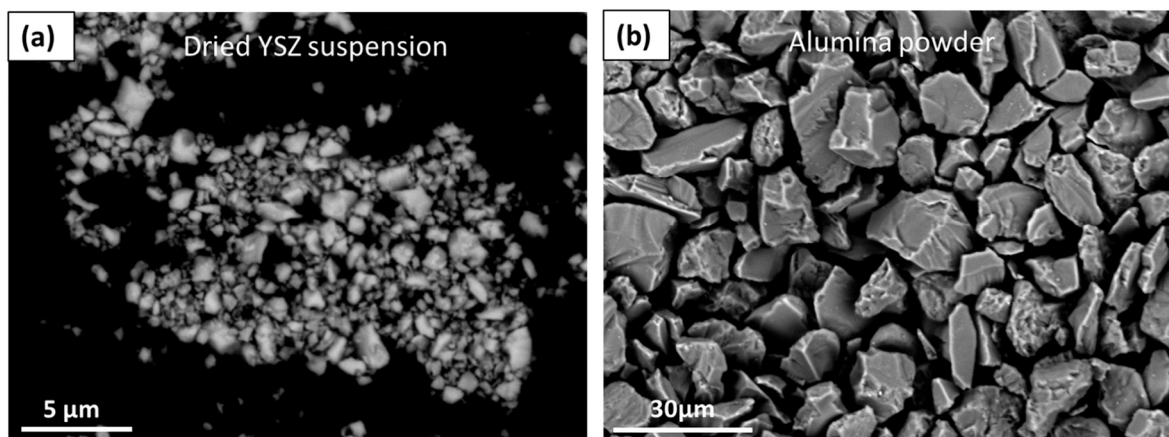
Fig. 1. Morphology of (a) 8YSZ powder (diluted & dried suspension) and (b) alumina powder.
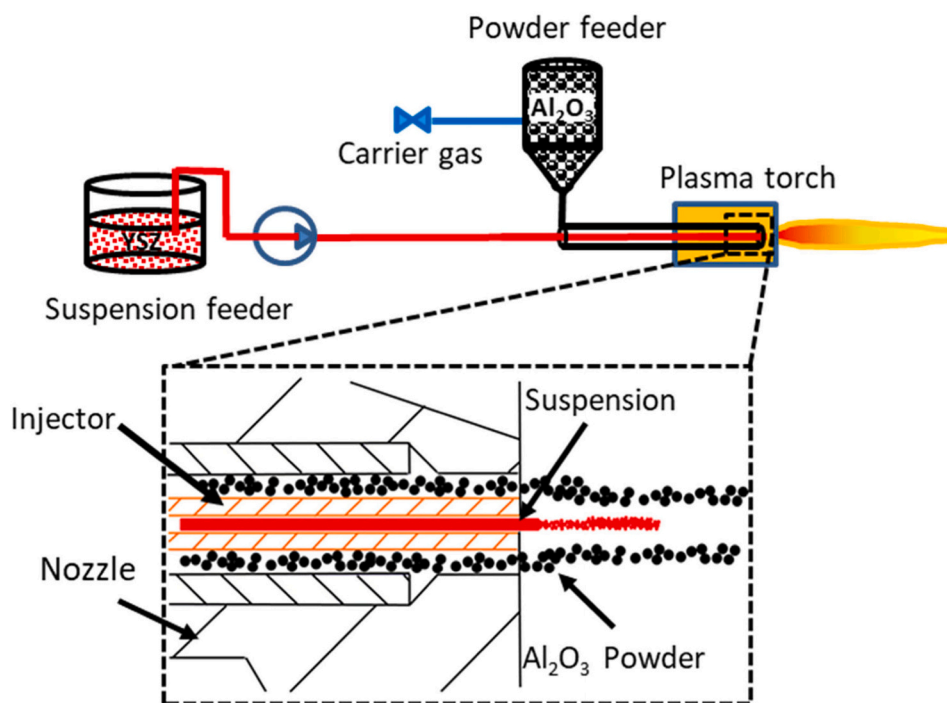

Fig. 2. Schematic showing hybrid powder-suspension spraying set-up utilized to deposit CMC coatings.

Table 1
Spray parameters used to deposit composite and monolithic coatings.

Parameters	Powder feed rate (g/min)	Suspension feed rate (mL/min)	Current (A)	Spray distance (mm)	Operating gas	Number of passes	Total gas flow (L/min)	Power (kW)
Monolithic	50	–	230	150	20H$_2$-80 N$_2$	20	180	109
CMC	50	10,22,35,50[a]	230	150	20H$_2$-80 N$_2$	12	180	109

[a] Feed rate corresponding to 5,10,15, 20 wt% YSZ and Al$_2$O$_3$ as balance in hybrid feedstock, respectively.

specimens in a low viscosity epoxy resin to avoid cracking or pull-outs during the subsequent sectioning step. The transverse sectioning of the specimens was then carried out using an alumina cutting blade. The sectioned specimens were then cold mounted using vacuum impregnation which was followed by semi-automatic polishing of mounted specimens using a Buehler PowerPro 5000 (Buehler, USA) system. Additionally, the fractured surface of the coatings was also prepared by slicing the substrate down to 0.5 mm thickness followed by bending the specimens to detach the free-standing films from the substrate. Finally,

the free-standing coatings were fractured to reveal the fractured surface.

Microstructural investigation of as-sprayed polished & fractured cross-sections, the top surface morphologies of the as-sprayed and eroded coatings was carried out through tabletop SEM (HITACHI, TM3000) under backscattered electron (BSE) mode & a field emission SEM (Model: S43000SE/N, Hitachi, Japan). Prior to SEM investigation, the ceramic coated samples were gold sputtered. Porosity of the coatings was assessed from 20 cross-sectional SEM micrographs (taken at 500× magnification focusing throughout the coating thickness) using image

analysis (ImageJ software).

The phase constitution of the monolithic coating was analysed using an X-Ray diffractometer (PANalytical X'Pert PRO, Malvern Panalytical B.V., Almelo, EA, The Netherlands) with Cu Kα radiation (λ = 1.54 Å). Whereas the phase constitution of the composite coatings was analysed using a Power D8 Discover diffractometer (Bruker AXS, Germany) with Cu-Kα radiation. In addition, Electron Dispersive X-ray Spectroscopy (EDS) analysis of the composite coatings was performed using a Leo 1550 Gemini SEM equipped with an X-Max 20 mm Silicon Drift Detector and Oxford Instruments Aztec software (Oxford Instruments, UK).

Hardness was measured by Vickers micro-hardness testing (HMV-2, Shimadzu Corp., Japan) on the polished cross-section of the coatings using 100 g constant load applied for 15 s. The measurements were carried out in ambient conditions and the hardness values were averaged over 8 recorded indents for each coating. Fracture toughness of both the coatings were experimentally measured in an earlier work and the details can be found here [28].

2.2. Coating wear performance

The as-sprayed CMC (alumina with 20 wt% YSZ) and Monolithic (alumina only) coatings showed different surface roughness, i.e., 11 ± 1 μm and 8 ± 2 μm, respectively. To study the tribological response of the inherent CMC and Monolithic coatings without the surface roughness effects influencing the results, the coating surfaces were grinded and polished prior to testing to obtain an average similar surface roughness of <1 μm (Ra). Three different types of tribological tests were performed to ascertain their tribological behaviour as described below, where scratch and dry sliding wear tests were conducted on polished surface whereas the erosion test was conducted on the as-sprayed surface.

2.2.1. Scratch test

A commercial automated scratch tester, CSEM Revetest, equipped with a Rockwell C diamond stylus (cone apex angle 120°, tip radius 200 μm) was used for scratch testing the polished coating specimens at ambient air condition. Linear scratches were made under progressive loading condition. The load was varied from 0 to 130 N. The loading rate was 100 N/min, with the stylus scanning the coating surface at a speed of 10 mm/min. A sensor mounted on the indenter holder was used to monitor and record the acoustic emission signal from the scratching action and subsequently relate it to damage in the coating. Post scratch examination of the coatings was done using Optical Microscopy (OM) (Nikon, Tokyo, Japan) and Stereo Microscopy (SM) (Nikon SMZ800N, Sweden).

2.2.2. Sliding wear test

A ball-on-plate tribometer (VTT, Finland) was used in dry sliding contact conditions to assess the dry sliding friction and wear resistance of both the CMC as well as Monolithic coatings studied in this work using a dense sintered 6 mm diameter Al_2O_3 sphere as the counter-surface. The test was performed at 10 N normal load with a sliding speed, total sliding distance, and radius (r), of the wear track as 0.1 ms^{-1}, 157 m, and 2.5 mm, respectively. Post wear analysis was done by determining the surface topography using Wyko NT1100 optical profiling system which was also used to create a 3D profile and corresponding 2D profile of the transverse section of the wear track. Calculation of the worn area was based on this 2D profile. Measurements were recorded at two diametrically opposite locations on each wear track after removing wear debris using an air jet. The worn areas at the two locations were determined from the wear track profiles and these were then averaged to ascertain the 'mean worn area'. The total volume loss of the wear track was then calculated as the product of the mean worn area and circumference of wear track (2πr). The wear rate of the coatings was then evaluated using the following formula:

$$Wear\ rate \left(\frac{mm^3}{Nm}\right) = \frac{Total\ volume\ loss\ of\ the\ wear\ track\ (mm^3)}{Force\ (N)*Total\ sliding\ distance\ (m)}$$

2.2.3. Erosion test

Erosion tests were carried out at room temperature using dry sand erosion test rig designed as per ASTM G76. Silica particles of mean particle size 200 ± 10 μm with angular morphology were used as erodent media. The test was carried out under similar conditions on both the coatings where the erodent feed rate, nozzle to sample distance and test duration were 4.5 g/min, 10 mm and 1 min, respectively. Erosion behaviour of the coatings were evaluated under two different erodent particle velocities (48 ms^{-1} and 108 ms^{-1}) and two impact angles (30°, 90°). Such study is also expected to provide possible insights about the ductile/brittle behaviour of the coatings. The erosion rate (which is the ratio of mass loss of the coatings to the erodent mass used to promote the erosion) was calculated. The weight loss was measured before and after testing using a weighing scale having a resolution of 0.01 mg (Model: Sartorius, Germany).

3. Results & discussion

3.1. Coating characterization

3.1.1. Microstructure and porosity analysis

The polished cross-sections of all the coatings studied in this work are shown in Fig. 3. The micrographs clearly reveal incorporation of white (YSZ) features in a grey (Al_2O_3) matrix. The reason for depositing coatings with varied YSZ content was primarily to demonstrate the successful utilization of the hybrid plasma spraying concept where a second phase having very fine size can be successfully incorporated in a coarse matrix. By simply adjusting the suspension feed rate during coating deposition, the hybrid processing route can produce composite coating with varied amount of second phase. As demonstrated in this work and shown in Table 1 the suspension feed rate was varied as 10, 22, 35 & 50 (mL/min) along with Al_2O_3 powder (feed rate 50 g/min) to produce 5, 10, 15 & 20 wt% YSZ reinforced Al_2O_3 composite coatings, respectively.

For detailed assessment of such hybrid processed composite coatings and evaluation of their tribological performance, the coating with the highest YSZ content (Al_2O_3-20YSZ), which is henceforth referred to as 'CMC' coating, was selected for further detailed investigation along with a coating without YSZ referred to as 'Monolithic' coating. The reason for selecting the composite coating with the highest YSZ content (20 wt%) was because of its significance in achieving superior tribological properties. As reported in the literature by Gafur et al. [38], the incorporation of YSZ in alumina can decrease the coating hardness but it can increase the facture toughness. Although the incorporation of YSZ in alumina can decrease the coating hardness, the resultant increase in the facture toughness of the composite coating can have a remarkable improvement in the tribological properties of the coating [35].Fig. 4 shows the SEM pictures of the top-surface (a), polished-cross-section (b) and fractured cross-section (c) of the CMC coating. The top-view image clearly shows the presence of white coloured YSZ splats (marked with the black arrows) and the grey coloured alumina splats (marked with the white arrows) which can also be observed in the polished as well as the fractured cross-section micrographs. Moreover, the polished and fractured cross-sections also show the presence of porosity (marked with dotted circles). Typical lamellar structured grains which are characteristic of conventional powder feedstock plasma sprayed coatings can also be seen from the fractured cross-section image (marked with white arrows). An important point to be noted is the size difference between the white YSZ splats and grey alumina splats from all the SEM micrographs shown in Figs. 3 and 4. The white YSZ splats/features appear to be several orders of magnitude smaller than the grey splats/features, which is consistent with the original mean particle size difference between the
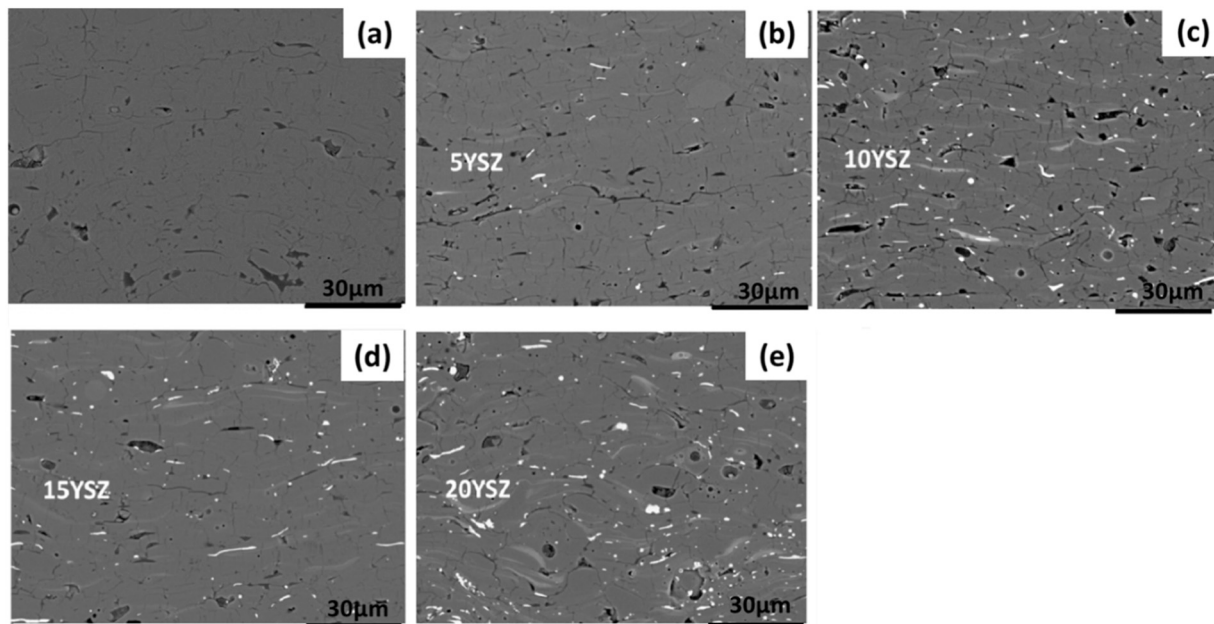
Fig. 3. Cross-section SEM images of the as-sprayed (a) Monolithic and CMC coatings with (b) 5 wt% YSZ, (c) 10 wt% YSZ, (d) 15 wt% YSZ and (e) 20 wt% YSZ in alumina matrix, respectively.
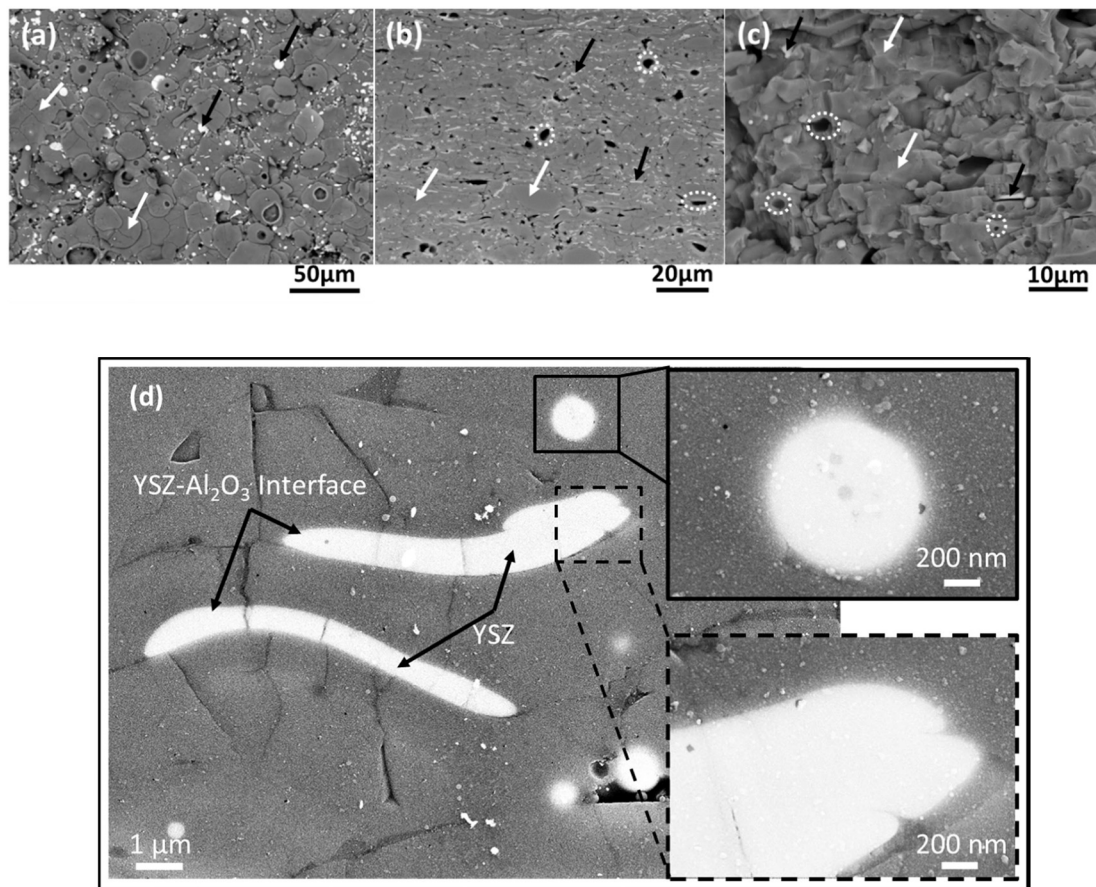

Fig. 4. SEM micrographs of the 20 wt% YSZ reinforced alumina matrix CMC coating: (a) top surface morphology, (b) polished cross-section and (c) fractured cross-section (white arrows: alumina splats/features, black arrows: YSZ splats/features, white dotted circles: pores and cracks).

two feedstocks, i.e., the Al_2O_3 powder (d50 ≈ 17 μm) and the YSZ suspension (d50 ≈ 400 nm). The presence of two dimensionally very distinct types of "building blocks" (splats) is indeed the key inherent and

potentially advantageous feature of coatings derived using a powder-suspension hybrid feedstock. Very high magnification secondary electron SEM images were also captured to study the interface of the Al_2O_3

and YSZ splats. A smooth interface between the Al_2O_3 and YSZ splats can be observed from Fig. 4(d) suggesting a good cohesion within the CMC coating.

The thickness and the porosity of both the Monolithic as well as the CMC coatings are reported in Table 2. The porosity in the CMC coating was slightly higher as compared to the Monolithic coating. This was is due to the relatively less specific energy available in the plasma plume while depositing CMC coating because of considerable energy being consumed in evaporating the solvent from the suspension feedstock. Despite of the lower specific energy in the plasma plume, the molten splats for alumina are a clear indicator for complete melting as observed in top surface morphologies from Fig. 4(a) ((marked by white arrows). However, the fine YSZ feedstock with higher melting point than alumina could have experienced significant less specific energy to form molten splats resulting in the formation of unmelted YSZ particles as evident from the fractured cross-section which could have contributed to the increased porosity.

Significant higher material deposition rate was achieved through the hybrid route as seen from the coating thicknesses per pass. The higher thickness per pass in case of the CMC coating was not surprising as an additional feedstock i.e., YSZ suspension was fed with 50 mL/min feeding rate along with 50 g/min alumina powder. On the contrary, during deposition of the Monolithic coating only 50 g/min alumina powder was fed under similar spray conditions. Despite of lower material deposition rate as demonstrated by the thickness per pass (see Table 2), the Monolithic coating was significantly thicker due to the significantly higher number of plasma torch passes (20) used to deposit the coating (see Table 1) compared to the CMC coating (12 passes, see Table 1).

3.1.2. Phase analysis by EDS and XRD

The EDS spot analysis of the CMC coating, as shown in Fig. 5, confirms the predominant presence of mainly zirconium in the white region (Spot 2) and aluminium in the grey region (Spot 1), attributable to the YSZ and alumina, respectively.

X-ray diffraction was carried out to identify the presence of the phases in the monolithic as well as CMC coatings and the corresponding XRD plots are shown in Fig. 6. In addition, the XRD plot for the alumina powder feedstock used for depositing Monolithic as well as CMC coating is also shown in Fig. 6(a) as a reference. The as-sprayed CMC coating contained a mixture of alpha (α) and gamma (γ) alumina phases, along with the presence of tetragonal zirconia (t-ZrO_2) and negligible (only one small peak) cubic Y_2O_3 phases. The alpha (α) phase is attributed to unmelted/partially melted alumina powder particles or to the molten powder particles which cooled at lower rate, whereas the nucleation of the metastable gamma (γ) as well as the formation of amorphous phase is associated with the rapid cooling of the molten splats at the substrate surface [39].

Since the starting alumina powder feedstock was pure alpha (α) alumina as shown in Fig. 6(a), the presence of gamma (γ) alumina phase in the CMC coating suggests that not all the powder particles were fully molten retaining some alpha (α) phase from the feedstock. Literature has shown that conventional plasma sprayed alumina coatings deposited under similar spray conditions consist of mainly gamma (γ) alumina phase due to the complete melting of the alumina powder particles which, upon rapid quenching transform from alpha (α) alumina into gamma (γ) alumina or amorphous phase [28]. Similar behaviour was

also noted for the Monolithic coating deposited in this work where mainly the presence of gamma (γ) alumina phase peaks can be seen (see Fig. 6(a)). Nevertheless, in this study, the CMC coating was processed using a hybrid route which involved an additional feedstock (YSZ) in the form of a suspension along with the alumina powder feedstock. Therefore, as explained earlier the availability of the plasma energy exclusively for heating the pure alpha (α) alumina powder feedstock was significantly reduced due to the usage of a substantial amount of the available plasma energy to evaporate the solvent (ethanol) from the suspension feedstock. Moreover, for both the Monolithic as well as the CMC coating studied in this work peaks of amorphous phase (between 40° to 70°) were observed, which has also been previously reported in literature especially for the conventional Monolithic plasma sprayed coatings where it is believed that extremely fast quenching rates in the plasma spray process allows the formation of such an amorphous phase in these coatings [16]. Although the energy available for melting alumina for producing CMC coating is reduced compared to producing Monolithic coating, significant energy was available for the case of CMC coating by virtue of employing a high energy Axial III plasma torch. This is evident from the reasonably low porosity and presence of mostly gamma phase in the CMC coating. Therefore, it should be further mentioned that the present hybrid route is promising while capitalizing on the high-power capability of the advanced plasma torch used in the present study.

3.2. Mechanical properties

The hardness and fracture toughness values of the CMC coating are reported in Table 2 and compared with those of the Monolithic coating. Rapid solidification of the molten corundum (α-Al_2O_3) alumina particles leads to the formation of meta-stable γ-Al_2O_3 in plasma sprayed alumina coatings, which exhibit lower hardness as compared to the coating comprising of pure corundum (α-Al_2O_3) [40,41]. As discussed earlier, the extent of melting of the corundum (α-Al_2O_3) alumina powder particles while depositing the CMC coating was not as significant as in case of depositing the Monolithic coating due to the use of plasma energy consumed for evaporating the solvent during CMC deposition. This allowed to retain larger traces of the harder corundum (α-Al_2O_3) phase in the CMC coating as compared to the Monolithic coating which was mainly consisting of the softer γ-Al_2O_3 and amorphous Al_2O_3 phases. Despite of this, the hardness of the CMC coating was found to be lower (1096 HV) than the monolithic coating (1361 HV). This could primarily be caused by the presence of higher porosity as well as the softer second phase (YSZ) in the CMC coating as the inherent bulk hardness of the porosity as well as the YSZ is significantly lower than alumina [42]. In addition, the presence of YSZ splats in the CMC coating resulted in numerous alumina-YSZ interfaces which could have also reduced the coating hardness since these are typically the weaker regions present in a coating.

In contrast to the hardness, the mean fracture toughness values of the CMC coating as shown in Table 2 were found to be significantly higher (about 4-fold) than in the Monolithic coating. Such a drastic difference in fracture toughness despite the higher porosity and larger traces of harder and brittle (α-Al2O3) phase in the CMC coating can mainly be attributed to the incorporation of a tougher second phase (YSZ) which successfully arrest the crack propagation.

Table 2
Coating characteristics of the Monolithic and CMC coatings studied in this work.

Coating ID	Surface roughness (as-sprayed, Ra) (μm)	Porosity (% area fraction)	Thickness (μm)	Thickness per pass (μm/pass)	Hardness (HV0.1)	Fracture toughness[a] (MPa·m$^{0.5}$)	Specific wear rate (10^6 μm^{3}N^{-1})
Monolithic	8 ± 2	2.2 ± 0.3	374.50 ± 13.65	19	1361 ± 100	2	0.55
CMC	11 ± 1	3.3 ± 0.5	356.92 ± 8.10	30	1096 ± 136	9	0.35

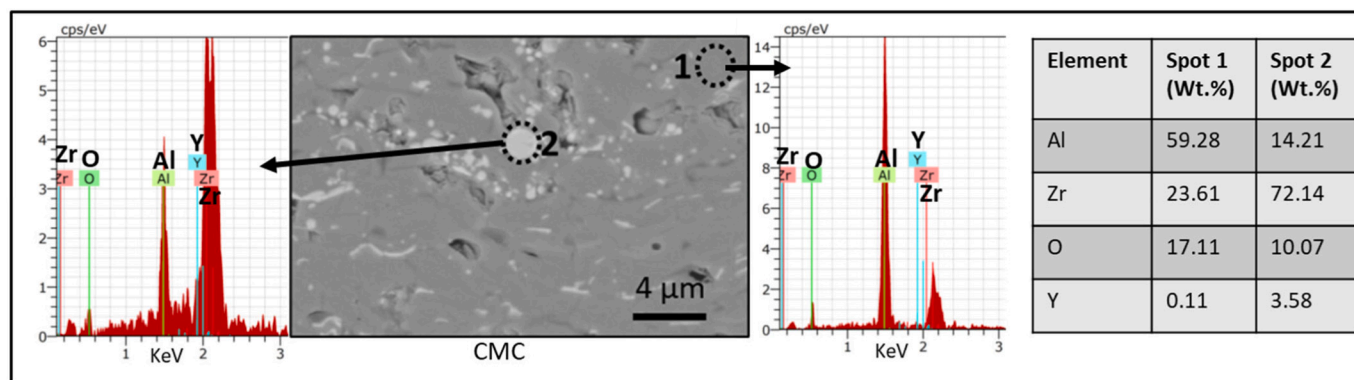[a] Fracture toughness values are taken from earlier work performed on similar coatings [28].

Fig. 5. EDS analysis of the CMC coating showing the presence of Zr-rich white phase distributed in an Al rich grey matrix.
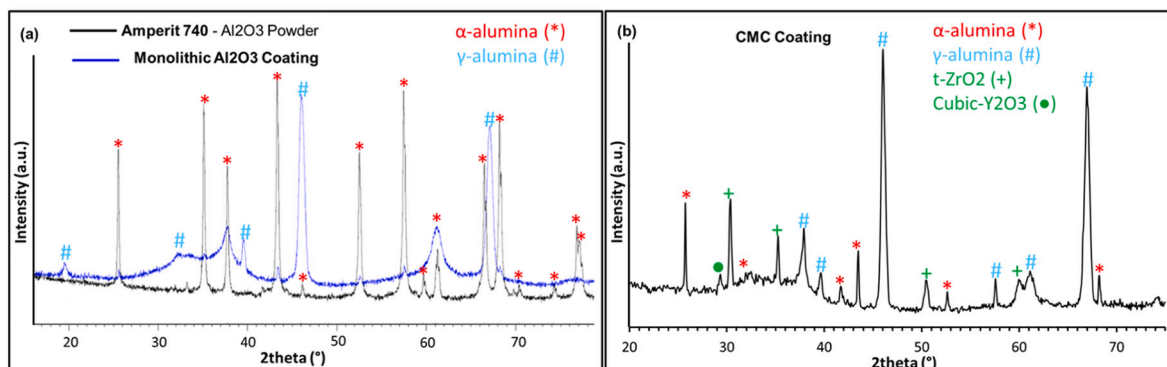

Fig. 6. XRD pattern of the alumina powder & monolithic coating (a) as well as the hybrid processed CMC coating (b) showing the presence of various phases i.e. Gamma (γ) alumina, Alpha (α) alumina, Tetragonal (t-ZrO_2) & cubic Y_2O_3.

3.3. Wear performance

3.3.1. Wear resistance during scratch test

The acoustic emission signals from the scratch test are plotted against the load and shown in Fig. 7(a). The significant increase in the acoustic emission signal at a lower load (around 60 N and onwards) suggests that the Monolithic coating experienced damage at a lower load compared to the CMC coating which showed an increase in the signal at a higher load (around 100 N and onwards). The optical micrographs of the wear tracks between 73 N to 83 N after the scratch tests, shown in Fig. 7(b and c) reveal that the width of the scratch track including the damage in its vicinity was less than half for the CMC coating (~200 μm) compared to the Monolithic coating (~500 μm), thereby supporting the acoustic signal observation. Similar observation was made in the 3D topography SEM pictures around the same region as shown in Fig. 7(d and e) as well as in the back scattered 2D SEM images as shown in Fig. 7 (f and g). Furthermore, Fig. 7(d, e, & g) also reveal the extent of damage after scratch test where extensive damage near the scratch track in the Monolithic coating can be observed as compared to the CMC coating.

As discussed by Bull et al. [43] the coating damage can show either brittle or ductile or both behaviours during scratch testing which can be easily distinguished from one another with the help of *post facto* image analysis. During the ductile behaviour the area of damage is confined primarily in the vicinity of the scratch track whereas during the brittle behaviour the damage extends far beyond the scratch track resulting in wider damage area. Moreover, the recorded acoustic emission signal curve during the scratch test is also used to distinguish between these two damage behaviours where a smooth curve suggests ductile whereas noisy curve with larger peaks suggests brittle behaviour. As can be seen from Fig. 7(a), the failure in the Monolithic coating was mostly brittle at all the loads whereas in case of the CMC coating, it was mixed of brittle

and ductile with brittle failure dominating only at higher loads (>100 N). Furthermore, as can be seen from Fig. 7(b, d & f) and (c, e & g), the damage area can be seen to be extending far wider than the shiny white scratch track in case of the Monolithic coating as compared to in the CMC coating which suggests a reduced brittle failure around this load in the CMC coating. This can be understood when remembering that the CMC coating is many times tougher which enhances the overall wear resistance as compared to the more brittle and harder Monolithic coating.

To further understand the mixed failure mode in the CMC coating, the high magnification SEM image was captured within the damaged area around 100 N which is shown in Fig. 8(a). Few among several damage modes proposed by Bull et al. [43] during scratch testing of the coatings for both brittle as well as the tensile failure behaviours are observed in case of the CMC coating which are shown in the SEM micrograph (Fig. 8(a)) as well as in the schematic (Fig. 8(b)). These damage modes are spallation, tensile cracking, and conformal cracking. The large area spallation occurs due to the poor cohesion within that region which can be due to the presence of higher localized porosity and delaminations. Conformal as well as tensile cracks also tend to be associated with the cohesive failure of the coating. Since the coating deforms with the ductile substrate, large bending stresses are induced at the sides of the scratch track, resulting in conformal and tensile cracks emerging from the edges of the scratch [43]. The conformal cracks follow semi-circular trajectories parallel to the leading edge of the indenter which form as the indenter deforms the coating and the underlying substrate. This results in tensile bending moments within the coating as it is pushed down underneath the indenter. Although, the tensile cracking failure mode appears seemingly like the conformal cracking, the semi-circular crack traces are parallel to the trailing edge of the indenter in tensile cracking, i.e., mirror images of the conformal
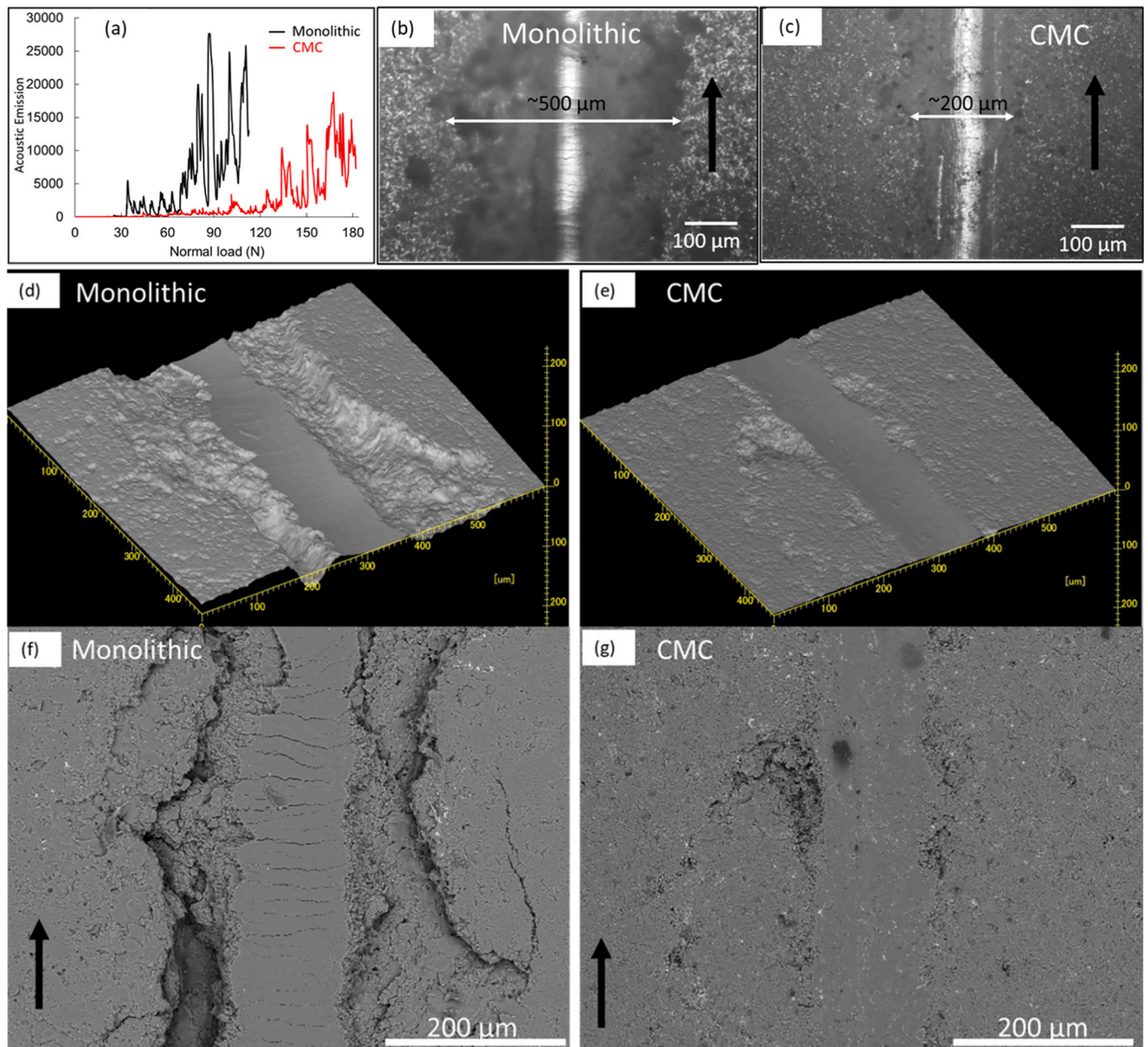
Fig. 7. Acoustic emission signals of scratches on the Monolithic and hybrid CMC coating (a) and 2D as well as 3D scratch tracks using optical microscopy & SEM in the load range 78–83 N normal load for (b, d & f) Monolithic (c, e & g) CMC coating. (The loading direction is shown by the black arrows.)

cracking. These cracks form because of the tensile frictional stresses present behind the trailing edge of the stylus balancing the compressive frictional stresses ahead.

3.3.2. Wear resistance under ball-on-plate dry sliding wear test

The specific wear rate for both the coatings is reported in Table 2. A significant reduction in the specific wear rate of the CMC coating compared to the Monolithic coating clearly demonstrates the benefit of the addition of YSZ as second phase on the wear performance of the coating. The 3D profiles and the corresponding 2D line scan at the centre of the 3D profile of the wear tracks for both the Monolithic and CMC coatings are also shown in Fig. 9(a and a-1) and (b and b-1), respectively, where about 30% lower maximum depth of the worn-out region in the CMC coating as compared to the Monolithic coating further confirms the CMC coating's superior wear behaviour. The superior wear resistance of the CMC coating can be related to the enhanced fracture toughness of the CMC coating due to the incorporation of the tougher second phase

(YSZ).

Post facto SEM images were also captured for both the Monolithic (Fig. 9(a-2)) as well as the CMC (Fig. 9(b-2)) coatings to better understand the wear mechanisms under dry ball on-plate wear test. Both the coatings showed mixed tensile and brittle/abrasive failure behaviour resulting due to the plastic flow as well as splat pull-out fracture, respectively. The predominant wear mechanism in the Monolithic coating can be seen to be of the brittle/abrasive type causing the material to delaminate/pull-out owing to the high pressure exerted by the alumina ball on the coating. However, the extent of brittle/abrasive failure can be seen to be lower in the CMC coating as evident from its rather smooth worn-out surface as compared to the Monolithic coating where the worn-out surface looks rather rough. The presence of porosity and delaminations play a significant role in aggravating the splat to delaminate or pull-out encouraging the brittle fracture by providing viable locations with higher stress concentration for crack initiation. However, the presence of tougher YSZ splats assist in inhibiting the
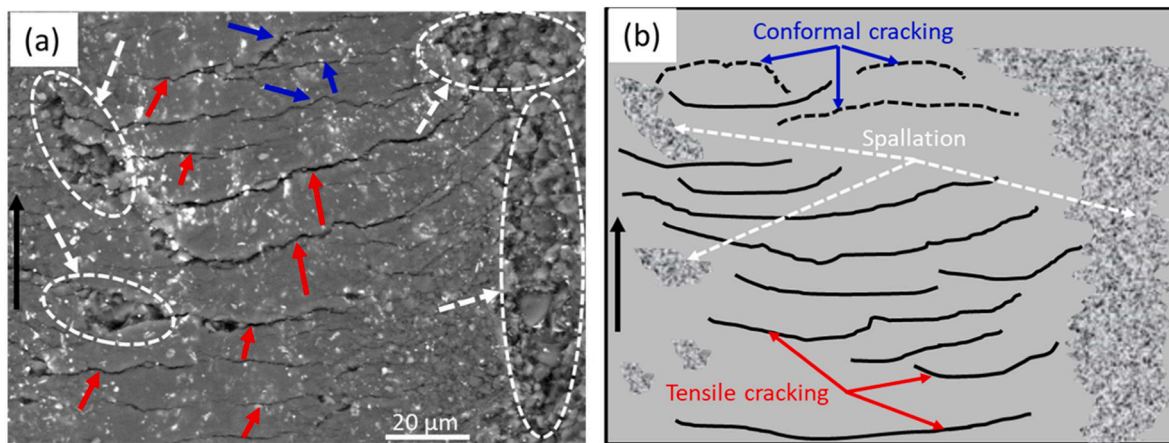
Fig. 8. Various damage modes in the CMC coating showing spallation (marked with the dotted white circle/arrows), tensile cracking (marked with red arrows) and conformal cracking (marked with blue arrows) in the SEM image (a) and the corresponding schematic (b) (The loading direction is shown by the black arrow).
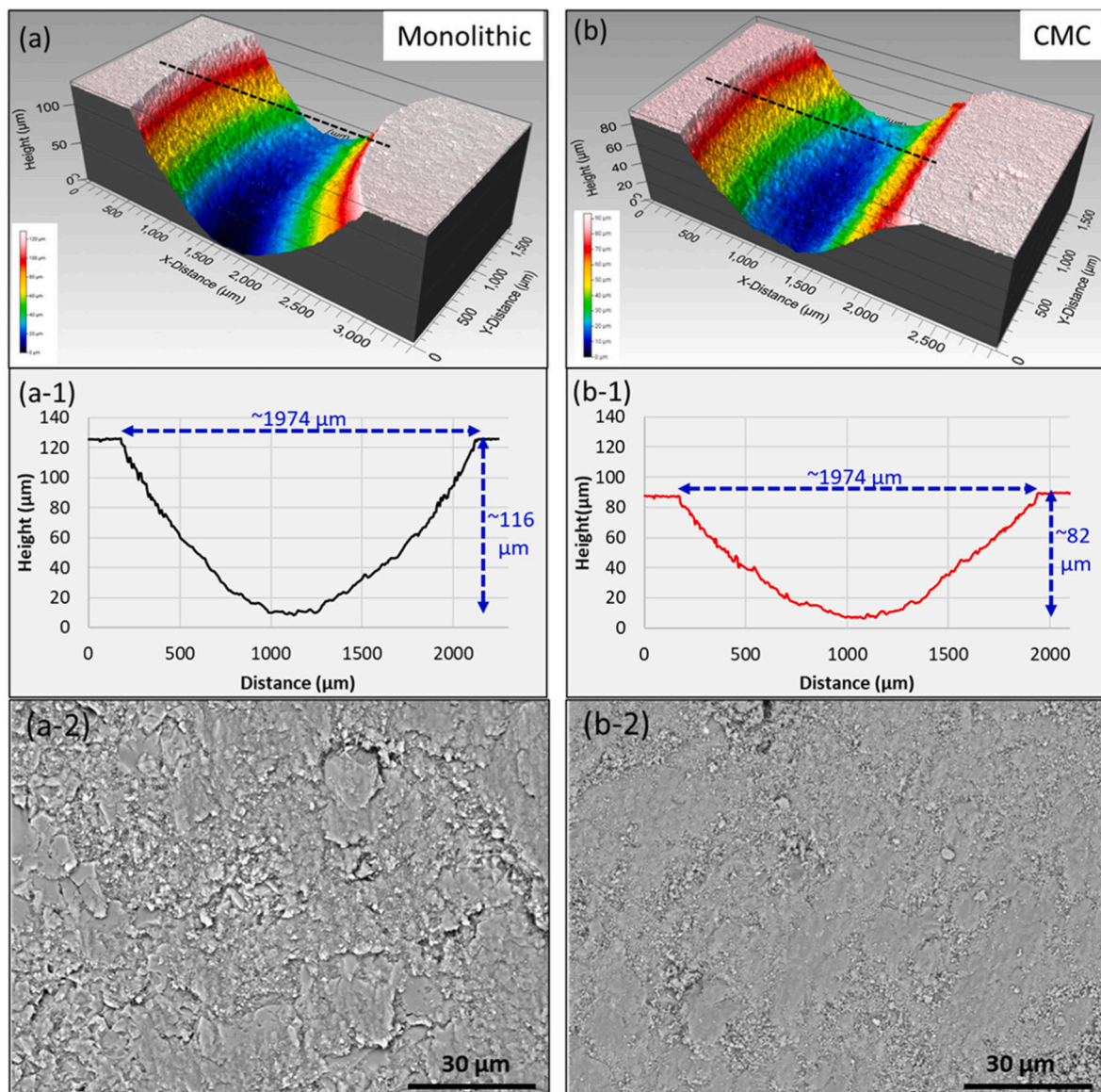

Fig. 9. 3D profilometry pictures of the wear tracks ((a) and (b)) along with the respective 2D line scans ((a-1) and (b-1)) captured along the black dotted line as marked in the 3D profiles and SEM images of the wear tracks ((a-2) and (b-2)) for the Monolithic and CMC coatings, respectively.

crack propagation receding the brittle fracture as well as the overall wear damage of the CMC coating.

3.3.3. Erosion wear resistance

The erosion behaviour of both the coatings was analysed and the results are summarized in Fig. 10. It is evident from Fig. 10(a) and (b) that the CMC coating had a better erosion resistance at both impact angles (90° & 30°) as well as at different erodent particle impact velocities (48 m/s & 108 m/s). The extent of erosion for both the CMC as well as the Monolithic coating can be seen to increase with the increase in the impact velocity at both impact angles. Moreover, the extent of erosion at different impact angles which is demonstrated by the ratio (see Fig. 10(c)) of erosion rate at higher impact angle to the erosion rate at lower impact angle can be seen to increase with the increase in the impact velocity in case of Monolithic coating. Because both constituents of the coatings being brittle ceramic, it is interesting to observe the extent of brittleness increases with increase in erodent velocity for Monolithic coating. However, the CMC exhibited similar brittle behaviour even at higher impact velocities exhibiting better integrity under harsh conditions too. The marginal increase can be noted for the CMC coating implying better toughness of the CMC coating as compared to the Monolithic coating.

To further understand the coating failure behaviour due to the erosive wear, *post facto* SEM images of the damaged regions were captured and are shown in Fig. 11. The SEM micrographs clearly reveal an uneven/rougher damaged surface attributable to the brittle failure in case of the Monolithic coating as compared to the CMC coating which shows a rather smoother damaged surface, and the difference is even more obvious at higher impact velocity. Such a difference in the damaged surface regions among two coatings is because of the higher hardness and lower toughness of the Monolithic coating which may increase the brittleness in the coating and hence adversely affect the coatings erosion behaviour with quick material removal from the coating due to brittle fracture.

The lower toughness of the Monolithic coating leads to the low erosion resistance whereas the higher toughness of the CMC coating due to the presence of uniformly dispersed small-sized YSZ as second phase leads to higher erosion resistance. It is well documented that higher toughness imparted by the YSZ in brittle alumina matrix is related to the transformation of metastable t-ZrO_2 into m-ZrO_2 in the stress field at a crack tip. This transformation exerts local compressive stresses, due to a volume expansion, hindering further crack propagation [44]. Therefore, superior toughness of the CMC coating may be related to the finely dispersed tetragonal and monoclinic ZrO_2 particles/splats in the alumina matrix, as also reported by Claussen et al. [45]. Accumulation of micro-cracks from the inter-splats and other micro-defects such as pores/cracks into a larger spallation crack and their subsequent propagation could be avoided due to the presence of fine ZrO_2 splats increasing the overall coating toughness and resulting in reduced brittle failure and improved erosive wear resistance of the CMC coating.

The mechanism of erosive wear in the CMC coating is also illustrated schematically and compared with that of the Monolithic coating in Fig. 12. The impact of the erosive media on the coating surface initiates cracks at the weaker regions such as splat boundaries, delaminations or pores as shown in Fig. 12(b) and (e), which have the tendency to propagate under constant erosive impact. The cracks propagate deeper in the Monolithic coating removing more material due to the brittle fracture as shown in Fig. 12(c). Whereas, in case of the CMC coating the presence of tougher YSZ phase can significantly absorb the impact energy from the erodent media and resist the crack initiation which can delay the coating spallation as shown in Fig. 12(e and f). Moreover, the cracks initiated at weaker regions in the alumina matrix in the CMC coating may also get arrested at the YSZ splats and hence terminate the crack with no further propagation as shown in Fig. 12(e and f) leading to significantly less material removal in the CMC coating.

4. Conclusions

This study aimed to demonstrate the hybrid processing route using a high-power axial injection plasma torch to deposit an Al_2O_3-YSZ CMC coating with multiple length scales for tribological applications. The incorporation of a fine second phase (YSZ) was found to be beneficial in enhancing the wear resistance under scratch, dry sliding ball-on-plate and erosion tests as compared to the conventional APS deposited monolithic Al_2O_3 coating. About 36% decrease in the dry sliding ball-on-plate specific wear rate and up to 50% decrease in the erosion wear rate was noted in the hybrid powder-suspension Al_2O_3-YSZ CMC coating as compared to the conventional APS deposited monolithic Al_2O_3 coating. The improved wear resistance under different tribological tests for the CMC coating was attributed to the coatings' microstructural features and resultant hardness & fracture toughness values. The hardness of the CMC coating was found to be lower (1096 HV) than the monolithic coating (1361 HV). This could primarily be caused by the presence of higher porosity as well as the softer second phase (YSZ) in the CMC coating. Despite higher porosity and the presence of retained alpha-alumina phase in the CMC coating, the toughness was found to be higher for the CMC coating (about 4-fold than monolithic) due to the reinforcement of the fine sized YSZ. In case of scratch as well as sliding wear tests conducted in this work, the wear mechanisms for both the CMC as well as the Monolithic coating were found to be a combination of the ductile failure occurring due to the plastic flow as well as the brittle fracture occurring due to the splat/grain pull-out and delamination. However, the extent of the brittle facture in the Monolithic coating was dominant compared to the CMC coating during both the scratch as well as sliding wear test. On the contrary, in case of the erosion testing, the wear mechanism for both the Monolithic as well as CMC coatings was predominantly brittle/abrasive fracture.

CRediT authorship contribution statement

1. Ashish Ganvir, Analysis of all the results & Writing-Original draft of manuscript.
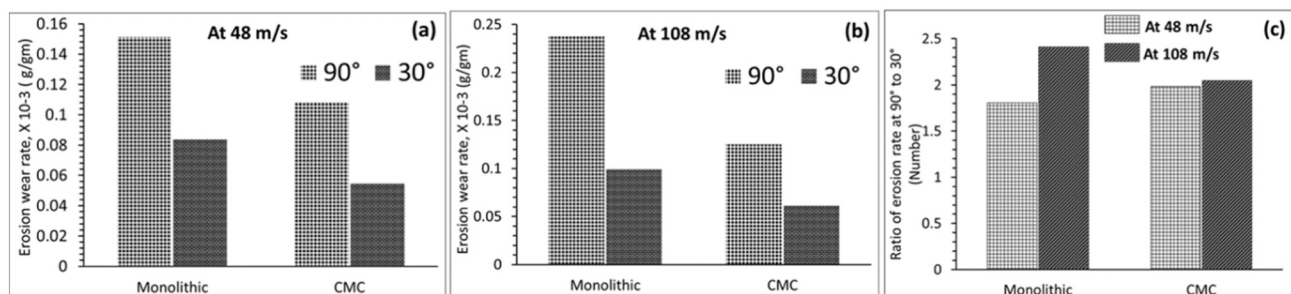

Fig. 10. Erosion rates of both Monolithic and CMC coatings at two different impact angles (90° & 30°) and two different impact velocities (48 m/s (a) and 108 m/s (b)) as well as the ratio of erosion rate at higher impact angle to the erosion rate at lower impact angle for both the impact velocities (c).
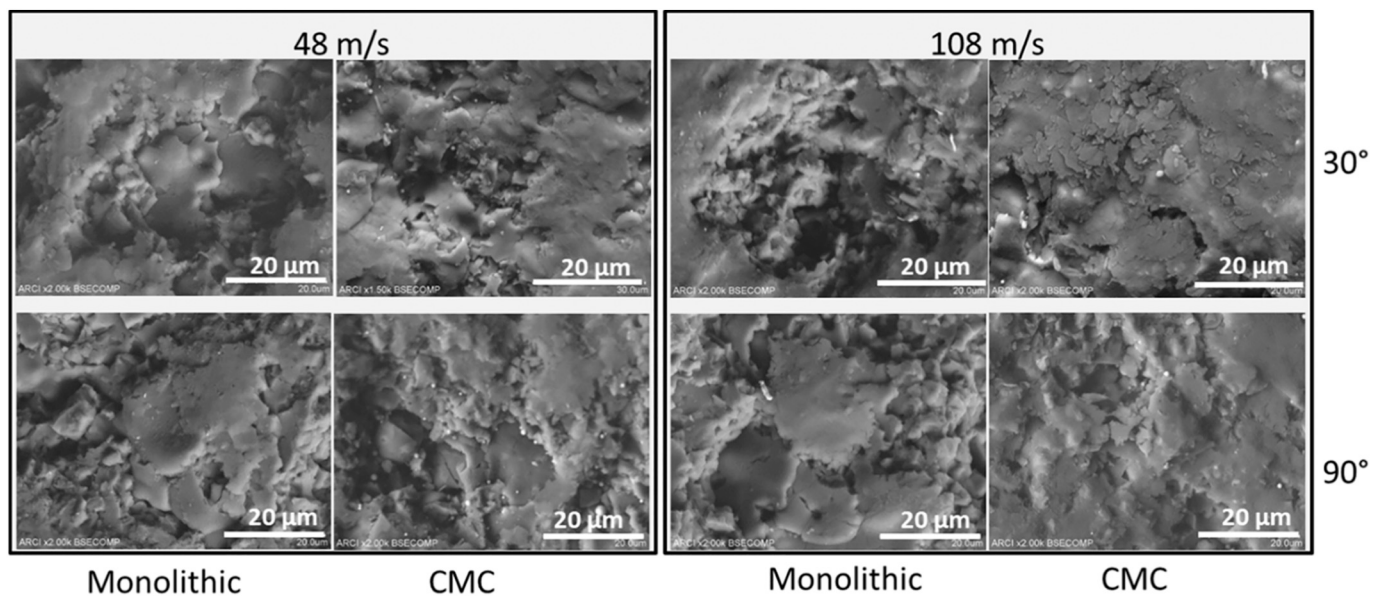
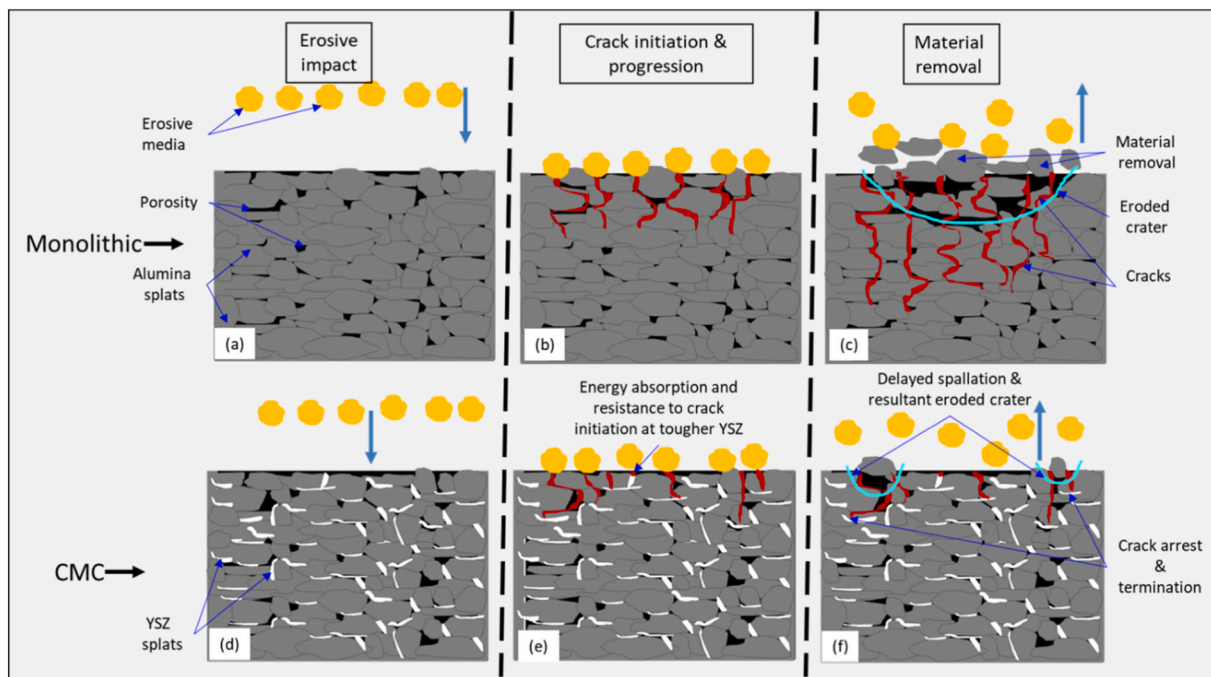**Fig. 11.** SEM images of the eroded regions in the coatings at different impact velocities and impact angles.

Fig. 12. Schematic representation of the erosive wear failure mechanism for Monolithic (a to c) and CMC (d to f) coatings.

Declaration of competing interest

The authors declare that they have no known competing financial interests or personal relationships that could have appeared to influence the work reported in this paper.

Acknowledgements

References

[1] V.P. Singh, A. Sil, R. Jayaganthan, A study on sliding and erosive wear behaviour of atmospheric plasma sprayed conventional and nanostructured alumina coatings, Mater. Des. 32 (2) (Feb. 2011) 584–591, https://doi.org/10.1016/j.matdes.2010.08.019.

[2] M. Karger, R. Vassen, D. Stover, Atmospheric plasma sprayed thermal barrier coatings with high segmentation crack densities: spraying process, microstructure and thermal cycling behavior, Surf. Coat. Technol. 206 (1) (Oct. 2011) 16–23, https://doi.org/10.1016/j.surfcoat.2011.06.032.

[3] R.K.S. Gautam, U.S. Rao, R. Tyagi, High temperature tribological properties of Ni-based self-lubricating coatings deposited by atmospheric plasma spray, Surf. Coat. Technol. 372 (Aug. 2019) 390–398, https://doi.org/10.1016/j.surfcoat.2019.05.024.

[4] J.-W. Chen, K.-Y. Lin, Y.-C. Yang, and S.-T. Yeh, "Plasma-sprayed LSM protective coating on metallic interconnect of SOFC," Coatings, vol. 7, no. 12, Art. no. 12, Dec. 2017, doi: https://doi.org/10.3390/coatings7120226.

[5] R.B. Heimann, Characterization of as-plasma-sprayed and incubated hydroxyapatite coatings with high resolution techniques, Mater. Werkst. 40 (1–2) (2009) 23–30, https://doi.org/10.1002/mawe.200800373.

[6] H. Liao, B. Normand, C. Coddet, Influence of coating microstructure on the abrasive wear resistance of WC/Co cermet coatings, Surf. Coat. Technol. 124 (2) (Feb. 2000) 235–242, https://doi.org/10.1016/S0257-8972(99)00653-2.

[7] M.M. Verdian, K. Raeissi, M. Salehi, Corrosion performance of HVOF and APS thermally sprayed NiTi intermetallic coatings in 3.5% NaCl solution, Corros. Sci. 52 (3) (Mar. 2010) 1052–1059, https://doi.org/10.1016/j.corsci.2009.11.034.

[8] Z. Zhou, L. Wang, D.Y. He, F.C. Wang, Y.B. Liu, Microstructure and electrochemical behavior of Fe-based amorphous metallic coatings fabricated by atmospheric plasma spraying, J. Therm. Spray Technol. 20 (1) (Jan. 2011) 344–350, https://doi.org/10.1007/s11666-010-9570-4.

[9] D. Zois, A. Lekatou, M. Vardavoulias, I. Panagiotopoulos, A. Vazdirvanidis, A comparative microstructural investigation of nanostructured and conventional Al2O3 coatings deposited by plasma spraying, J. Therm. Spray Technol. 17 (5) (Dec. 2008) 887–894, https://doi.org/10.1007/s11666-008-9268-z.

[10] S. Sathish, M. Geetha, S.T. Aruna, N. Balaji, K.S. Rajam, R. Asokamani, Sliding wear behavior of plasma sprayed nanoceramic coatings for biomedical applications, Wear 271 (5) (Jun. 2011) 934–941, https://doi.org/10.1016/j.wear.2011.03.023.

[11] Y. Wang, G. Darut, T. Poirier, J. Stella, H. Liao, M.-P. Planche, Cavitation erosion of plasma sprayed YSZ coatings produced by feedstocks with different initial sizes, Tribol. Int. 111 (Jul. 2017) 226–233, https://doi.org/10.1016/j.triboint.2017.03.019.

[12] Q. Wang, C.S. Ramachandran, G.M. Smith, S. Sampath, Sliding wear behavior of air plasma sprayed Al2O3 coatings sealed with aluminum phosphate, Tribol. Int. 116 (Dec. 2017) 431–439, https://doi.org/10.1016/j.triboint.2017.08.002.

[13] P.P. Bandyopadhyay, D. Chicot, B. Venkateshwarlu, V. Racherla, X. Decoopman, J. Lesage, Mechanical properties of conventional and nanostructured plasma sprayed alumina coatings, Mech. Mater. 53 (Oct. 2012) 61–71, https://doi.org/10.1016/j.mechmat.2012.05.006.

[14] R.S. Lima, A. Kucuk, C.C. Berndt, Bimodal distribution of mechanical properties on plasma sprayed nanostructured partially stabilized zirconia, Mater. Sci. Eng. A 327 (2) (Apr. 2002) 224–232, https://doi.org/10.1016/S0921-5093(01)01530-1.

[15] C. Lamuta, G. Di Girolamo, L. Pagnotta, Microstructural, mechanical and tribological properties of nanostructured YSZ coatings produced with different APS process parameters, Ceram. Int. 41 (7) (Aug. 2015) 8904–8914, https://doi.org/10.1016/j.ceramint.2015.03.148.

[16] X. Song, T. Suhonen, T. Varis, L. Huang, X. Zheng, Y. Zeng, Fabrication and characterization of amorphous alumina-yttria-stabilized zirconia coatings by air plasma spraying, J. Therm. Spray Technol. 23 (8) (2014) 1302–1311, https://doi.org/10.1007/s11666-014-0124-z.

[17] S. Goel, S. Björklund, N. Curry, U. Wiklund, and S. Joshi, "Axial suspension plasma spraying of Al2O3 coatings for superior tribological properties," Surf. Coat. Technol., vol. 315, no. Supplement C, pp. 80–87, Apr. 2017, doi: https://doi.org/10.1016/j.surfcoat.2017.02.025.

[18] A. Ganvir, S. Joshi, N. Markocsan, R. Vassen, Tailoring columnar microstructure of axial suspension plasma sprayed TBCs for superior thermal shock performance, Mater. Des. 144 (Apr. 2018) 192–208, https://doi.org/10.1016/j.matdes.2018.02.011.

[19] A. Ganvir, R.F. Calinas, N. Markocsan, N. Curry, S. Joshi, Experimental visualization of microstructure evolution during suspension plasma spraying of thermal barrier coatings, J. Eur. Ceram. Soc. 39 (2) (Feb. 2019) 470–481, https://doi.org/10.1016/j.jeurceramsoc.2018.09.023.

[20] S. Björklund, S. Goel, S. Joshi, Function-dependent coating architectures by hybrid powder-suspension plasma spraying: injector design, processing and concept

[21] H. Hou, J. Veilleux, F. Gitzhofer, Q. Wang, Y. Liu, Hybrid suspension/solution precursor plasma spraying of a complex Ba(Mg1/3Ta2/3)O3 perovskite: effects of processing parameters and precursor chemistry on phase formation and decomposition, J. Therm. Spray Technol. 28 (1) (Jan. 2019) 12–26, https://doi.org/10.1007/s11666-018-0797-9.

[22] S.V. Joshi, G. Sivakumar, Hybrid processing with powders and solutions: a novel approach to deposit composite coatings, J. Therm. Spray Technol. 24 (7) (Oct. 2015) 1166–1186, https://doi.org/10.1007/s11666-015-0262-y.

[23] A. Lohia, G. Sivakumar, M. Ramakrishna, S.V. Joshi, Deposition of nanocomposite coatings employing a hybrid APS + SPPS technique, J. Therm. Spray Technol. 23 (7) (Oct. 2014) 1054–1064, https://doi.org/10.1007/s11666-014-0071-8.

[24] F. Cipri, F. Marra, G. Pulci, J. Tirillò, C. Bartuli, T. Valente, Plasma sprayed composite coatings obtained by liquid injection of secondary phases, Surf. Coat. Technol. 203 (15) (May 2009) 2116–2124, https://doi.org/10.1016/j.surfcoat.2008.09.029.

[25] M. Mistri, S. Joshi, K.K. Kar, K. Balani, Tribomechanical insight into carbide-laden hybrid suspension-powder plasma-sprayed Tribaloy T400 composite coatings, Surf. Coat. Technol. 396 (Aug. 2020) 125957, https://doi.org/10.1016/j.surfcoat.2020.125957.

[26] S. Mahade, S. Björklund, S. Govindarajan, M. Olsson, S. Joshi, Novel wear resistant carbide-laden coatings deposited by powder-suspension hybrid plasma spray: characterization and testing, Surf. Coat. Technol. 399 (Oct. 2020) 126147, https://doi.org/10.1016/j.surfcoat.2020.126147.

[27] V. Gopal, S. Goel, G. Manivasagam, and S. Joshi, "Performance of hybrid powder-suspension axial plasma sprayed Al2O3—YSZ coatings in bovine serum solution," Materials, vol. 12, no. 12, Art. no. 12, Jan. 2019, doi: https://doi.org/10.3390/ma12121922.

[28] J.W. Murray, A. Leva, S. Joshi, T. Hussain, Microstructure and wear behaviour of powder and suspension hybrid Al2O3–YSZ coatings, Ceram. Int. 44 (7) (May 2018) 8498–8504, https://doi.org/10.1016/j.ceramint.2018.02.048.

[29] J. Oberste Berghaus, J.-G. Legoux, C. Moreau, F. Tarasi, T. Chráska, Mechanical and thermal transport properties of suspension thermal-sprayed alumina-zirconia composite coatings, J. Therm. Spray Technol. 17 (1) (Mar. 2008) 91–104, https://doi.org/10.1007/s11666-007-9146-0.

[30] N. Dejang, A. Limpichaipanit, A. Watcharapasorn, S. Wirojanupatump, P. Niranatlumpong, S. Jiansirisomboon, Fabrication and properties of plasma-sprayed Al2O3/ZrO2 composite coatings, J. Therm. Spray Technol. 20 (6) (Dec. 2011) 1259–1268, https://doi.org/10.1007/s11666-011-9672-7.

[31] J. Chevalier, A.H.D. Aza, G. Fantozzi, M. Schehl, R. Torrecillas, Extending the lifetime of ceramic orthopaedic implants, Adv. Mater. 12 (21) (2000) 1619–1621, https://doi.org/10.1002/1521-4095(200011)12:21<1619::AID-ADMA1619>3.0.CO;2-O.

[32] F. Kern, P. Palmero, Microstructure and mechanical properties of alumina 5vol% zirconia nanocomposites prepared by powder coating and powder mixing routes, Ceram. Int. 39 (1) (Jan. 2013) 673–682, https://doi.org/10.1016/j.ceramint.2012.06.078.

[33] R.V. Mangalaraja, B.K. Chandrasekhar, P. Manohar, Effect of ceria on the physical, mechanical and thermal properties of yttria stabilized zirconia toughened alumina, Mater. Sci. Eng. A 343 (1) (Feb. 2003) 71–75, https://doi.org/10.1016/S0921-5093(02)00368-4.

[34] F. Kern, P. Palmero, F. G. Marro, and A. Mestra, "Processing of alumina–zirconia composites by surface modification route with enhanced hardness and wear resistance," Ceram. Int., vol. 41, no. 1, Part B, pp. 889–898, Jan. 2015, doi: https://doi.org/10.1016/j.ceramint.2014.09.006.

[35] F. Sommer, R. Landfried, F. Kern, R. Gadow, Mechanical properties of zirconia toughened alumina with 10–24vol.% 1Y-TZP reinforcement, J. Eur. Ceram. Soc. 32 (16) (Dec. 2012) 4177–4184, https://doi.org/10.1016/j.jeurceramsoc.2012.06.019.

[36] N. Krishnamurthy, M. S. Prashanthareddy, H. P. Raju, and H. S. Manohar, "A study of parameters affecting wear resistance of alumina and yttria stabilized zirconia composite coatings on Al-6061 substrate," ISRN Ceramics, Dec. 31, 2012. https://www.hindawi.com/journals/isrn/2012/585892/ (accessed Dec. 22, 2020).

[37] L. Marcinauskas, et al., Microstructure and tribological properties of plasma sprayed alumina and alumina-graphite coatings, Surf. Coat. Technol. 350 (Sep. 2018) 401–409, https://doi.org/10.1016/j.surfcoat.2018.06.081.

[38] M. A. Gafur, M. S. R. Sarker, M. Z. Alam, and M. R. Qadir, "Effect of 3 mol% yttria stabilized zirconia addition on structural and mechanical properties of alumina-zirconia composites," Mater. Sci. Appl., vol. 8, no. 7, Art. no. 7, Jun. 2017, doi: https://doi.org/10.4236/msa.2017.87041.

[39] R. McPherson, On the formation of thermally sprayed alumina coatings, J. Mater. Sci. 15 (12) (Dec. 1980) 3141–3149, https://doi.org/10.1007/BF00550387.

[40] T. Lampke, et al., Corrosion and wear behavior of alumina coatings obtained by various methods, Mater. Sci. 46 (5) (Mar. 2011) 591–598, https://doi.org/10.1007/s11003-011-9328-2.

[41] P. Nayar, et al., Structural, optical and mechanical properties of amorphous and crystalline alumina thin films, Thin Solid Films 568 (Oct. 2014) 19–24, https://doi.org/10.1016/j.tsf.2014.07.053.

[42] P. Ctibor, L. Kraus, J. Tuominen, P. Vuoristo, P. Chráska, Improvement of mechanical properties of alumina and zirconia plasma sprayed coatings induced by laser post-treatment, Ceramics − Silikáty 51 (4) (2007) 181–189.

[43] S.J. Bull, Failure modes in scratch adhesion testing, Surf. Coat. Technol. 50 (1) (Jan. 1991) 25–32, https://doi.org/10.1016/0257-8972(91)90188-3.

[44] V. Teixeira, A. Monteiro, J. Duarte, A. Portinha, Deposition of composite and nanolaminate ceramic coatings by sputtering, Vacuum 67 (3) (Sep. 2002) 477–483, https://doi.org/10.1016/S0042-207X(02)00235-X.

[45] N. Claussen, Fracture toughness of Al2O3 with an unstabilized ZrO2 dispersed phase, J. Am. Ceram. Soc. 59 (1–2) (1976) 49–51, https://doi.org/10.1111/j.1151-2916.1976.tb09386.x.